An Online Metric Learning-Based Open-Switch and Current Sensor Fault Diagnosis for MSPMSM Systems

Yutao Du, *Student Member, IEEE*, Chi Li, *Member, IEEE*, and Zedong Zheng, *Senior Member, IEEE*

***Abstract*—Rapid and accurate removal of faulty sectors is the conventional fault tolerance method for highly secure multisector permanent magnet synchronous motors (MSPMSMs). In this article, a new fault diagnosis method for MSPMSMs based on metric learning (ML) is proposed. Its advantage is that it can complete fault detection and faulty sector location within 0.1 current fundamental cycle, which is faster than previous methods. Meanwhile, for the faulty sector, 28 types of open switch faults and current sensor faults can be accurately identified. In addition, since the fault diagnosis is based on structural characteristics, the proposed method is independent of system parameters and naturally robust to the speed and current variation. Particularly, using the consistent structural characteristics of MSPMSM sectors, an amplitude-trend distance (ATD) is presented to obviously reflect the difference of the same phase currents between healthy and faulty sectors. Subsequently, to ensure the speed of fault detection and high false alarm immunity, the ATD value under different fault states is theoretically analyzed, and a reasonable threshold is set. Compared to traditional ML methods, which requires complex computational classification methods, four characteristic parameters sector, polar, close to zero, and sensor flag are developed to locate the faulty sector and the faulty switch or current sensor. The experiment results on four-sector permanent magnet synchronous motor (PMSM) verify the effectiveness of the proposed fault diagnosis method.**

***Index Terms*—Amplitude-trend distance (ATD), current sensor fault, fault diagnosis, metric learning (ML), multisector permanent magnet synchronous motor (MSPMSM), open-switch (OS) fault.**

I. Introduction

MULTISECTOR permanent magnet synchronous motor (MSPMSM) has the advantages of high reliability, high rated power, low requirement on rated power of power devices, and simple control algorithm, which can be used to improve the performance of motor drive system. As a result, MSPMSM is becoming the more attractive choice for areas with high power rating and reliability requirements, including electric vehicles, aerospace, and offshore wind power generation [1], [2], [3].

Motor system faults mainly include motor faults, driver faults, and sensor faults. According to industry statistics, 38% of faults are happened due to power inverters, and most of the remaining are reflected in power switch faults [4]. The power switch fault is mainly appearing as the short switch and open switch (OS) [5]. The short switch is usually caused by overvoltage, overheating, or abnormal given signals. Once this happens, it will cause a large overcurrent in a very short time, which generally causes devastating damage to the drive. In general, there are special hardware detection and protection circuits for short switch. In addition, the current sensor failure distorts the measurement signal, which can lead to performance degradation and even damage to other components. The fault modes of the current sensor mainly include zero-offset (ZO), gain-variation (GV), signal-loss (SL), and signal-stuck (SS) [6]. There are many fault-tolerant control methods to achieve motor stability and no torque fluctuation operation when the driver has the OS or the current sensor fault. However, for applications requiring high performance after failure, fault-tolerant control methods must know the exact location of the fault in advance. Meanwhile, with appropriate protection measures, timely detection and fault location can prevent further deterioration of minor faults and lead to rapid maintenance. Hence, OS and current sensor faults diagnosis in the MSPMSM system are essential.

Over the last decades, the fault diagnosis methods for switches or sensors can generally be classified as model-based methods, signal analysis methods, and data-driven methods [7], [8]. Model-based methods rely on the drive model to estimate signals. The difference between the estimated signal and the measured signal is used to distinguish whether the device is healthy or not. Observer-based methods, parameter estimation methods, and parity space techniques are the most typical model-based method [9], [10], [12].

Drive OS fault will lead to the distortion of current and voltage signals. Therefore, the fault diagnosis method through signal analysis is also very popular, which can be divided into the voltage-based method [13], [14] and the current-based method [15], [16]. The voltage-based fault diagnosis method needs to install voltage sensors and related circuits on the original driving

Manuscript received 28 October 2022; revised 3 February 2023; accepted 3 April 2023. Date of publication 10 April 2023; date of current version 19 May 2023. This work was supported in part by the China National Key R&D Program during the 14th Five-year Plan Period under Grant 2021YFB2500702 and in part by the National Natural Science Foundation of China under Grant U2106217. Recommended for publication by Associate Editor H. Chaoui. *(Corresponding author: Zedong Zheng.)*

The authors are with the State Key Laboratory of Power System, Department of Electrical Engineering, Tsinghua University, Beijing 100084, China (e-mail: duyt20@mails.tsinghua.edu.cn; chi.li.2014@ieee.org; zzd@tsinghua.edu.cn).

Color versions of one or more figures in this article are available at https://doi.org/10.1109/TPEL.2023.3265936.

Digital Object Identifier 10.1109/TPEL.2023.3265936

system. By measuring the voltage difference between the fault phase and the normal phase, the fault phase can be quickly identified and accurately located. The average current Park's vector method is a representative method of current signal analysis and diagnosis. By analyzing the average stator current, fault features are constructed based on the sectors contacted by the postfault current track, which generally requires a fundamental wave period for diagnosis [17], [18].

Machine learning technology has made remarkable progress in recent years. Extensive research focuses on data-driven drive fault diagnosis [19], [20], [21], [22]. By extracting the mapping relationship between measurement data and fault labels, the machine learning-based diagnosis model is trained offline. This well-trained model can generate diagnostic results based on input. In [23], manifold feature learning is used to generate fault features. Then, using the data from the source system, an extreme learning machine model is trained to diagnose inverter faults.

All the abovementioned methods can realize the fault diagnosis of the MSPMSM system, but each has several limitations. Model-based methods are highly dependent on the accuracy of model parameters. The risk of a false alarm is greatly increased when the parameter mutation or system disturbance occurs. Methods based on voltage signal analysis require additional sensors, significantly increasing the cost and complexity of the system. The method based on current signal analysis needs a relatively long diagnosis time to ensure high detection accuracy, generally one fundamental period. The data-driven method requires a large amount of historical data for training and a large amount of computation, which is difficult to be applied in the microprocessor.

It is worth noting that in some specific cases, current sensor and switch faults have the similar fault characteristics. For example, when the current sensor breaks or two switches of the same bridge open at the same time, the mathematical fault expression is similar. At present, few studies have been reported on the simultaneous identification of switch faults and current sensor faults. In [24], a method based on normalized average current is proposed to detect switch and current sensor faults of permanent magnet synchronous motor (PMSM). It can detect a variety of switch faults and distinguish current sensor faults from switch faults, but only applicable to the PMSM equipped with three-phase current sensors. Basically, in order to save cost, two-phase current sensors are installed to achieve normal control. In [25], a random vector functional link network-based fault diagnosis method for inverter switch and current sensor.

Since each sector of the multisector PMSM drive system can be regarded as an independent three-phase drive system, each sector can be independently diagnosed by the abovementioned methods. However, the consistent and independent structural characteristics of its subsectors provide a new idea for the design of fault diagnosis methods. Metric learning is one of the most attractive machine learning in recent years, which has been widely used in face verification, fingerprint recognition, and object quality detection [26], [27], [28]. The core idea of the algorithm is to design a measure to reflect the similarity degree between similar and dissimilar samples, and then use support vector machine (SVM), neural network (NN), or other methods

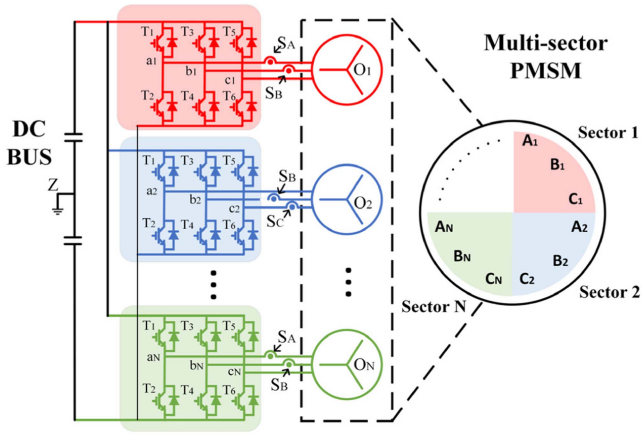

Fig. 1. *N*-sector PMSM drives system architecture.

for sample classification [29], [30]. Based on metric learning, Euclidean distance (ED) and improved cosine distance are used to diagnose PMSM drives [31] and multilevel converters [32], respectively.

This article proposes an online metric learning-based OS and current sensor faults diagnosis method for MSPMSM to shorten the fault detection and fault sector location time, which is extremely important for high-security MSPMSM applications. The major contributions are made as follows.

1) The new ATD with a known upper limit is designed. Compared with the traditional cosine distance and ED, the abnormal current amplitude and trend all lead to a decrease in ATD. This means a faster drop and a larger gap before and after faults.
2) To achieve a reliable threshold setting with a small tune effort, the current characteristics under different faults are analyzed theoretically, and the maximum and minimum values of ATD in different fault states are traversed. Based on ATD and reasonable threshold, fault detection is high immunity to the false alarm and faster than previous methods;
3) Compared with the ML-based on high compute burden classifiers, such as NN or SVM, the feature parameter sector is designed to locate the fault sector while detecting the fault. The feature parameters CTZ, polar, and SF are designed to accurately identify fault switches or current sensors;

The rest of this article is organized as follows. Section II introduces the MSPMSM system and fault diagnosis scheme. Section III expounds on the proposed ML-based fault detection and location method. Section IV is the experimental results and the performance comparison with previous methods. Finally, Section V concludes this article.

II. Structure of MSPMSM Drive System

The structure of *N*-sector PMSM with *N*-paralleled voltage source inverters (VSIs) is depicted in Fig. 1, which has *N*-independent neutral points. Each sector has the same phase and electrical parameters. The design of MSPMSM winding

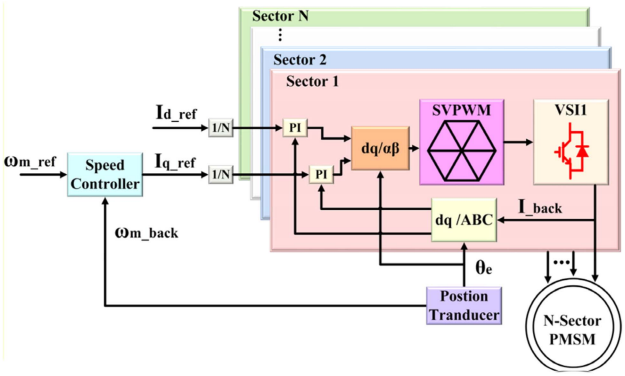

Fig. 2. Control scheme of *N*-sector PMSM.

displacement makes the mutual inductance between different three-phase winding sets become very low and can be ignored [33]. The magnetic decoupling between sectors means that each subsector motor can operate independently. Therefore, the fault of one subsector will only cause a relatively small part of torque ripple and has almost no influence on other subsectors. An independent VSI drives each subsector motor. This approach enables low-power inverters to drive high-power devices, reducing the overall inverter cost and ease of maintenance. When one parallel inverter fails, it does not affect the other inverter's dc–ac power conversion. In addition, to save cost, each subsector motor is equipped with two-phase current sensors. Because of the neutral constraint, the sum of the sector three phase currents is zero, which can obtain the phase current of the other phase.

The control scheme of *N*-sector PMSM is shown in Fig. 2. The control method of each subsector motor is the same as that of the traditional three-phase motor. Since the subsector motors share a rotor, all control loops share a speed regulator. Each sector inputs the same given currents, and 2*N* current loops output 2*N* reference voltage vectors. Finally, The *N* space vector pulsewidth modulation (PWM) output the PWM signals of the driver according to the input reference voltage vector and drives the *N* sector PMSM.

III. Structure of MSPMSM Drive System

The block diagram of the ML-based fault diagnosis method for the multisector PMSM drive system is shown in Fig. 3.

A sliding window is designed to collect the phase current of each sector at time *k*. The operating rules are shown in Fig. 4. The ATD measures the similarity of the phase current in different sectors. In this article, the similarity of phase currents between the first sector and other sectors is calculated. When the ATD is lower than the threshold, the Flag is set to 1. If either Flag becomes 1, the fault is detected. The fault sector can be identified according to Flag and Table II. After fault detection, CTZ, polar, and SF are calculated. The CTZ can distinguish whether the phase has a switch open, and the Polar can distinguish the upper switch, the lower switch, or the double switch is open. The SF is used to distinguish the double switch fault of the same bridge from the current sensor fault. The accurate fault location can be accomplished through CTZ, polar, SF, and Table III.

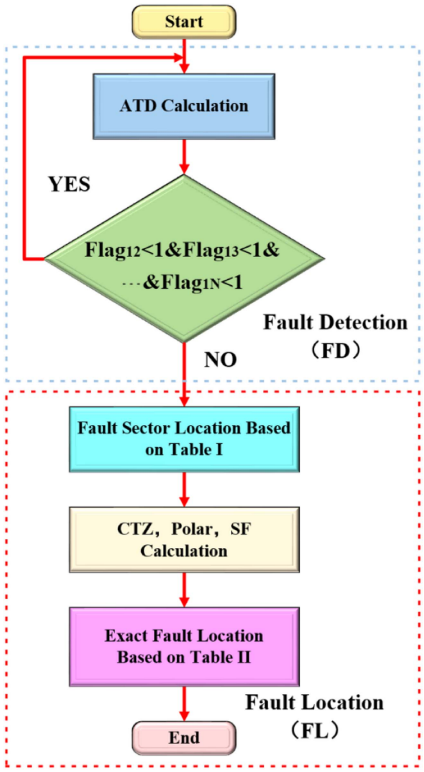

Fig. 3. Block diagram of proposed fault diagnosis method.

Fig. 4. Operation rule of the sliding windows.

TABLE I
Fault Sector Location Table

Sector	$Flag_{12}$	$Flag_{13}$	$Flag_{14}$	…	$Flag_{1n}$
0(healthy)	0	0	0	…	0
1	1	1	1		1
2	0	1	0	…	0
3	0	0	1	…	0
		⋮			
N	0	0	0	…	1

A. Similarity Measurements

Generally, there are two ways to measure the similarity of data. One is ED, and the other is cosine distance (CD). The ED of the same phase currents in different sectors can be written as

$$\mathrm{ED}_{x,mn}\left(i_{x,m}, i_{x,n}\right) = \left(\sum_{k=1}^{L} \left|i_{x,m}(k) - i_{x,n}(k)\right|^2\right)^{1/2}$$
$$(m, n = 1, 2, 3, \ldots, N; x = A, B, C) \quad (1)$$

TABLE II
EXACT FAULT LOCATION TABLE

Fault	$Polar_{A,N}$	$Polar_{B,N}$	$Polar_{C,N}$	$CTZ_{A,N}$	$CTZ_{B,N}$	$CTZ_{C,N}$
T1	-	0	0	1	0	0
T2	+	0	0	1	0	0
T3	0	-	0	0	1	0
T4	0	+	0	0	1	0
T5	0	0	-	0	0	1
T6	0	0	+	0	0	1
T1T2	0	0	0	1	0	0
T1T3	-	-	+	1	1	/
T1T4	-	+	0	1	1	/
T1T5	-	+	-	1	/	1
T1T6	-	0	+	1	/	1
T2T3	+	-	0	1	1	0
T2T4	+	+	-	1	1	/
T2T5	+	0	-	1	/	1
T2T6	+	-	+	1	/	1
T3T4	0	0	0	0	1	0
T3T5	+	-	-	/	1	1
T3T6	0	-	+	/	1	1
T4T5	0	+	-	/	1	1
T4T6	-	+	+	/	1	1
T5T6	0	0	0	0	0	1
others	0	0	0	0	0	0
A SL	SF_A=1					
B SL	SF_B=1					
C SL	SF_C=1					
A SS	SF_A=2					
B SS	SF_B=2					
C SS	SF_C=2					

TABLE III
FOUR SECTOR SYSTEM PARAMETERS

Parameters	Value	Parameters	Value
Motor sector	4	D-axis resistance	0.0818 [mH]
Inverter sector	8	Q-axis inductance	0.1972 [mH]
Switching frequency	10[kHz]	Phase resistance	5.15 [mΩ]
Pole pair number	4	Magnet flux linkage	0.279 [Wb]

where $i_{x,m/n}$ is the x phase current in sector m/n. ED can reflect the similarity of two current sample amplitudes. The larger value for $ED_{x,mn}(i_{x,m},i_{x,n})$ indicates that two-phase currents are distant and less similar.

The cosine distance of the same phase currents in different sectors can be written as

$$CD_{x,mn}\left(i_{x,m},i_{x,n}\right)=\frac{\sum_{k=1}^{L}\left(i_{x,m}(k)\cdot i_{x,n}(k)\right)}{\sqrt{\left(\sum_{k=1}^{L}i_{x,m}^{2}(k)\right)\cdot\left(\sum_{k=1}^{L}i_{x,n}^{2}(k)\right)}} \tag{2}$$

which can reflect the similarity of the two current sample trends. $CD_{x,mn}(i_{x,m},i_{x,n})$ is equal to 1 in a perfectly direct linear relationship. When the relationship is completely inverse linear, $CD_{x,mn}(i_{x,m},i_{x,n})$ is -1. The less relationship between the two phase currents, the $CD_{x,mn}(i_{x,m},i_{x,n})$ value is closer to 0.

Rearranging (1) and (2), ED and CD can be rewritten as (3) and (4). Considering that the two similarity measurement methods are complementary, the ATD is proposed as (5), shown at the bottom of the next page. which considers the amplitude and trend similarity of the two-phase current, and the upper limit is 1. The $ATD_{x,mn}(i_{x,m},i_{x,n})$ value of 1 means that the amplitudes of the two phases are equal and positively correlated. When the $ATD_{x,mn}(i_{x,m},i_{x,n})$ is closer to 0, the similarity between the two phase currents is smaller

$$CD'_{x,mn}\left(i_{x,m},i_{x,n}\right)=\frac{\sum_{k=1}^{L}\left(i_{x,m}(k)\cdot i_{x,n}(k)\right)}{\sqrt{\left(\sum_{k=1}^{L}i_{x,m}^{2}(k)\right)\cdot\left(\sum_{k=1}^{L}i_{x,n}^{2}(k)\right)}}\leq\frac{2\sum_{k=1}^{L}\left(i_{x,m}(k)\cdot i_{x,n}(k)\right)}{\sum_{k=1}^{L}\left(i_{x,m}^{2}(k)+i_{x,n}^{2}(k)\right)} \tag{3}$$

$$ED'_{x,mn}\left(i_{x,m},i_{x,n}\right)=\frac{1}{1+\left(\sum_{k=1}^{L}\left|i_{x,m}(k)-i_{x,n}(k)\right|^{2}\right)^{\frac{1}{2}}}. \tag{4}$$

B. ATD Value Analysis After OS or Sensor Faults

Current sensor ZO and GV have less impact on the motor drive system than SL and SS. Fig. 5 shows the comparison of feedback currents between the faulty and the health sector under lower switch fault, upper switch fault, double-switch fault, current sensor SL, and current sensor SS.

The current feedback of the healthy and fault sector can be separately expressed as (6) and (7), where A is the current amplitude, ω is the electric angular velocity, T_{fault} is the time that the fault causes current distortion, and C is the signal bias. When the switch fault or the current sensor SL appears, C is 0. In this article, the ratio Z of the sliding window current sampling frequency f_s to the current fundamental frequency f_c is 100, and the sliding window length is $L = 10$. When the 1/2 sampling points in the sliding window are the postfault current signal, the ATD value is calculated as the reference for threshold setting

$$I_{\text{healthy}}(t)=A\sin(\omega t) \tag{6}$$

$$I_{\text{fault}}(t)=\begin{cases}A\sin(\omega t) & 0\leq t\leq T_{\text{fault}}\\ C, & t\geq T_{\text{fault}}\end{cases}. \tag{7}$$

In Fig. 6, the current amplitude and offset can be expanded as required. Here, 15 A and ±2.5 A are used as examples. The maximum and minimum values of ATD under different current amplitudes and biases are traversed, as shown in Fig. 6.

C. Fault Detection and Fault Sector Location

The value of ATD is used to measure the similarity of in-phase currents in any two sectors. In the healthy state, the same phase current coincides, which results in the ATD being small. This is not true when a failure occurs. The current of the first sector is compared with the other sectors. When phase x of the n sector

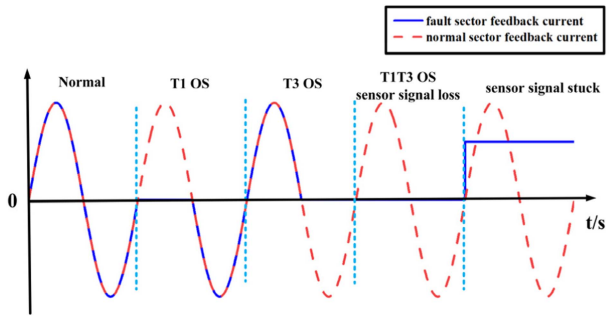

Fig. 5. Current feedback waveform comparison between the faulty and the healthy sector.

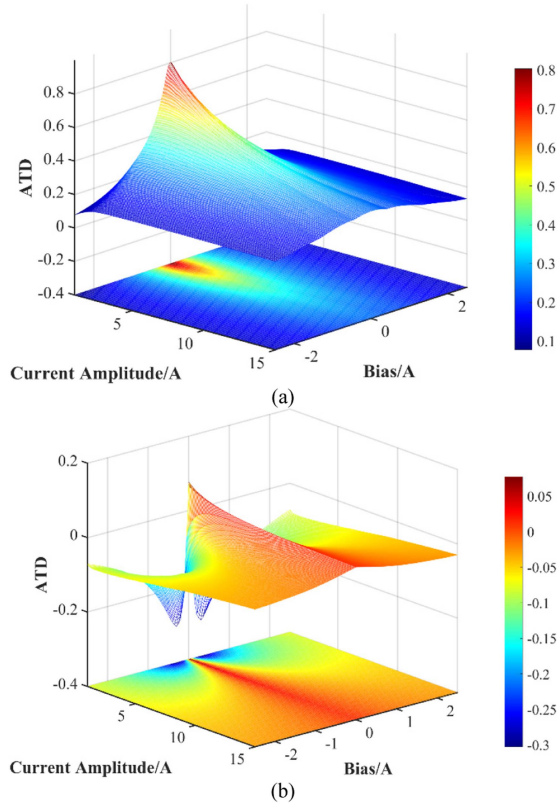

Fig. 6. ATD in different cases. (a) Maximum value. (b) Minimum value.

is faulty, $\mathrm{ATD}_{x,1n}$ will be less than the threshold K_{sim}, then the $\mathrm{Flag}_{x,1n}$ will be set to 1, which is written as

$$\mathrm{Flag}_{x,1n} = \begin{cases} 0, & \mathrm{ATD}_{x,1n} \geq K_{\mathrm{sim}} \\ 1, & \mathrm{ATD}_{x,1n} < K_{\mathrm{sim}} \end{cases}. \tag{8}$$

As a result, criterion of sector fault flag can be presented as

$$\mathrm{Flag}_{1n} = \mathrm{Flag}_{A,1n} | \mathrm{Flag}_{B,1n} | \mathrm{Flag}_{C,1n}. \tag{9}$$

When a fault happens in any phase, Flag_{1n} will appear as a value other than 0. Based on Flag_{1n}, the feature parameter sector is designed to preliminarily locate the fault sector, as shown in Table I. When the fault occurs in sector 1, the fault-phase current of this sector is significantly different from other sectors, and all the Flag_{1n} is 1. However, when the fault occurs in sector *n*, the current of the other sector is very similar to sector 1, resulting in Flag_{1n} as one and all others as zero.

D. Fault Exact Location

As shown in Fig. 5, after the OS occurs, the fault-phase current will remain 0 for some time in each fundamental period. The closed-to-zero current samples at *k* instant are defined as (10). The minimal threshold K_ε is predefined, $|H_{x,n}(k)| = 1$ means that the $i_{x,m}$(k) is close to zero

$$H_{x,n}(k) = \begin{cases} 1 & i_{x,n}(k) > K_\varepsilon \\ -1 & i_{x,n}(k) < -K_\varepsilon \\ 0 & \text{else} \end{cases}. \tag{10}$$

The percentage of current samples close to 0 in a sliding window can be written as

$$M_{x,n}(k) = \frac{1}{L} \sum_{j=k-L+1}^{k} |H_{x,n}(j)|. \tag{11}$$

If $M_{x,n}$ (k) is greater than a predefined threshold K_z, the characteristic parameter $\mathrm{CTZ}_{x,n}$ (k) of *x* phase in the *n* sector is set to 1, as shown in the following equation:

$$\mathrm{CTZ}_{x,n}(k) = \begin{cases} 0, & M_{x,n}(k) < K_z \\ 1, & M_{x,n}(k) \geq K_z \end{cases}. \tag{12}$$

With the $\mathrm{CTZ}_{x,n}$ (k), the fault can be further located in the faulty phase. Next, another characteristic parameter is used to identify whether the broken switch is upper or lower, as shown in (13). In a sliding window, the ratio of the sum to the absolute sum of the current samples is defined as $N_{x,n}$ (k). It represents the polarity of energy flowing through the *x* phase of the fault sector

$$N_{x,m}(k) = \sum_{j=k-L+1}^{k} H_{x,m}(j) \Bigg/ \left| \sum_{j=k-L+1}^{k} H_{x,m}(j) \right|. \tag{13}$$

The percentage of current samples polarity in a sliding window can be written as

$$\mathrm{Polar}_{x,n}(k) = \begin{cases} 1, & M_{x,n}(k) > K_\gamma \\ -1, & M_{x,n}(k) < -K_\gamma \\ 0, & \text{else} \end{cases}. \tag{14}$$

A value of 0 for $\mathrm{Polar}_{x,m}(k)$ indicates that the energy flowing through the upper and lower switches is equal in the faulty state, which means that both switches fail. The positive value of $\mathrm{Polar}_{x,m}(k)$ means that the energy flowing through the lower

$$\mathrm{ATD}_{x,mn}\left(i_{x,m}, i_{x,n}\right) = \frac{2\sum_{k=1}^{L}\left(i_{x,m}(k) \cdot i_{x,n}(k)\right)}{\left(1 + \left(\sum_{k=1}^{L} |i_{x,m}(k) - i_{x,n}(k)|^2\right)^{\frac{1}{2}}\right) \times \sum_{k=1}^{L}\left(i_{x,m}^2(k) + i_{x,n}^2(k)\right)}. \tag{5}$$

switch is less than the energy flowing through the upper switch, which means that the lower switch fails. On the contrary, the negative value of $\mathrm{Polar}_{x,m}(k)$ means that the energy flowing through the upper switch is less than the energy flowing through the lower switch, which means that the upper switch fails.

It should be noted that when $T1$ and $T2$ switches fail simultaneously, their characteristic parameters $\mathrm{CTZ}_{1,n}(k)$ and $\mathrm{Polar}_{1,n}(k)$ are consistent with the current sensor A phase SL, and the same is true when phase B and phase C fail. Therefore, the feature parameter SF is added, which can be expressed as

$$\mathrm{SF}_{x,n}(k) = \begin{cases} 1, |i_{x,n}(k-L+1)| < K_n \& \cdots \& |i_{x,n}(k)| < K_n \\ \quad |i_{x,n}(k-L+1)| \geq K_n \& \cdots \& |i_{x,n}(k)| \geq K_n \\ 2, \quad \& \\ \quad \mathrm{err}_{x,n}(k-L+1) < K_n \cdots \& \mathrm{err}_{x,n}(k) < K_n \\ 0, \text{else} \end{cases} \tag{15}$$

$$\mathrm{err}x,n(k) = |ix,n(k) - ix,n(k-1)|. \tag{16}$$

K_n is the sampling fluctuation threshold, which is much smaller than K_z. For current sensor SL and stuck faults, the current sampling feedback is basically stable at a fixed value. The fluctuations are much smaller than the sampling fluctuations caused by diode continuity and electromagnetic interference when the current sensor is healthy and the switch is opened.

Based on the abovementioned analysis, an exact fault location table of the fault sector is proposed as Table II, where / is the unconcerned condition. "Others" in the table means the current sensor A/B/C GV or ZO. After the fault is detected, the $\mathrm{SF}_{x,n}$ 1 and 2 represent the SL and stuck of the x phase current sensor, respectively. Then, the exact fault location is completed. If $\mathrm{SF}_{x,n}$ is 0 for ten sampling periods after the fault is detected, the SL and stuck of the current sensor can be excluded, and the remaining fault types can be located by CTZ and Polar.

E. Tuning Efforts

The tuning effort is an important feature of any algorithm, and the solution should have as little tuning as possible. The proposed fault diagnosis method needs six parameters, including ratio Z, criterion K_{sim}, K_ε, K_z, K_γ,, and K_n. In this article, $Z = 100$ is used for analysis and experiments, which is determined by the hardware conditions of the experimental platform. A larger L means faster fault detection and a lower false alarm rate. However, for lower L, the proposed method still has a great performance, which is proved by the following experiment. K_{sim} is used for fault detection and is recommended to be (17), where λ is a constant. Large λ means a short diagnosis time, while small λ means a low false alarm rate. The maximum and minimum values of ATD after the fault have been analyzed in Section B. In this article, λ is recommended 8, and the K_{sim} is calculated under different fault conditions, as shown in Fig. 7. Since the threshold is the largest when the bias is 0, the threshold is set according to this condition to simplify debugging. A larger θ_{zero} leads to a more robust fault diagnosis against transients, whereas a smaller θ_{zero} leads to a faster diagnosis. K_z is a sign to identify

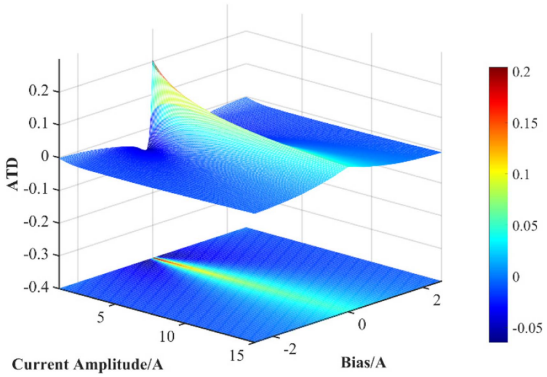

Fig. 7. Threshold reference in different cases.

the fault phase. In the healthy state, there are very few current samples close to zero in a fundamental period, but after the OS or current sensor SL, the current samples will be zero for at least half a period. K_γ measures the polarity of the sampling current flowing through the fault phase. A larger K_γ means faster fault classification, and a smaller K_γ means a lower misclassification rate. K_n is the sampling fluctuation threshold, and its value is much smaller than K_z based on good hardware design. In fact, although the proposed fault diagnosis method is designed with seven feature parameters, only four parameters, θ_{zero}, K_z, K_γ , and K_n need to be tuned.

$$K_{\mathrm{sim}} = \frac{\lambda \mathrm{ATD}_{\min} + \mathrm{ATD}_{\max}}{\lambda + 1} \frac{\mathrm{ATD}_{\max} + \mathrm{ATD}_{\min}}{\mathrm{ATD}_{\max} - \mathrm{ATD}_{\min}} \tag{17}$$

$$K_\varepsilon = A_m \sin(\theta_{\mathrm{zero}}). \tag{18}$$

IV. Experimental Results

The following analysis is entirely based on experimental results, as they better describe the performance of the algorithm in the presence of nonideal characteristics, such as the differences between sectors caused by the manufacturing process, measurement noise, dead-zone effects. The performance of the proposed fault diagnosis method is evaluated according to some indicators, such as detection and fault sector location time, and robustness. Taking A phase of the first sector fault as an example, five kinds of faults are carried out, including single switch open fault, two switches open fault in the same phase, two switches open fault in different phases, SL of A phase current sensor, and GV of A phase current sensor, which are represented by T1, T1T2, T1T4, sensor A SL, and sensor A GV, respectively. The performance of the fault diagnosis method under different current amplitudes, different sampling frequencies, the current step, and the speed reference step is also analyzed. The experimental results are represented by FD and FL, which displays the results of fault detection and exact fault location, respectively.

A four-sector PMSM is implemented in an eight-sector drive based on TMS320F28377D. The experimental setup shown in Fig. 8 consists of the four-sector PMSM, dc source, real-time interface, oscilloscope, controller, and inverter. The main motor and inverter parameters are shown in Table III. The values of

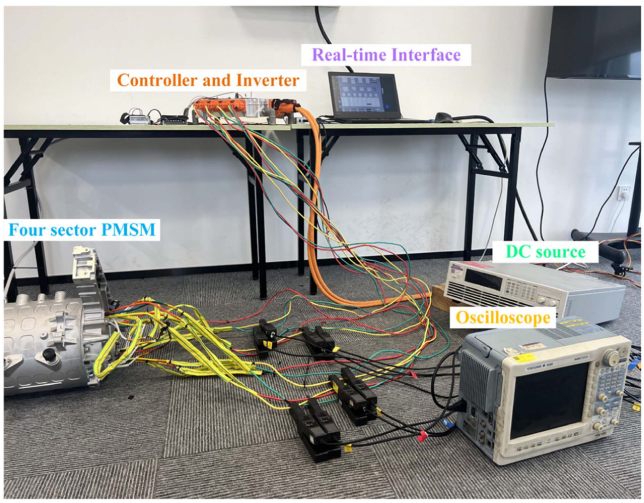

Fig. 8. Four-Sector PMSM system.

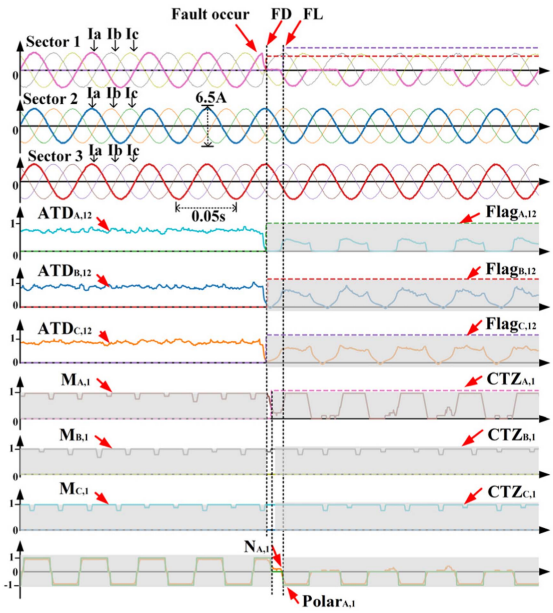

Fig. 9. Fault diagnosis process when T1 open circuit.

θ_{zero}, K_z, $K_{\gamma,}$, and λ for fault diagnosis are set as 0.05, 0.3, 0.4, and 8, respectively, while K_{sim} is online adaptive.

A. Single OS Fault Diagnosis

Fig. 9 shows the diagnosis process of the first sector T1 switch open-circuit fault. Subfigure 1 demonstrates the three-phase currents in sectors 1, 2, and 3. The gray area indicates that the relevant parameters do not need to be calculated, and the display is only for ease of understanding. The phase and amplitude of the current in the healthy sector are the same. Due to the baud rate limitation of the real-time interface, only the second and the third sector three-phase currents are shown in the figure. In the healthy state, the current difference between each sector is very small. When the first sector is faulty, the phase current will

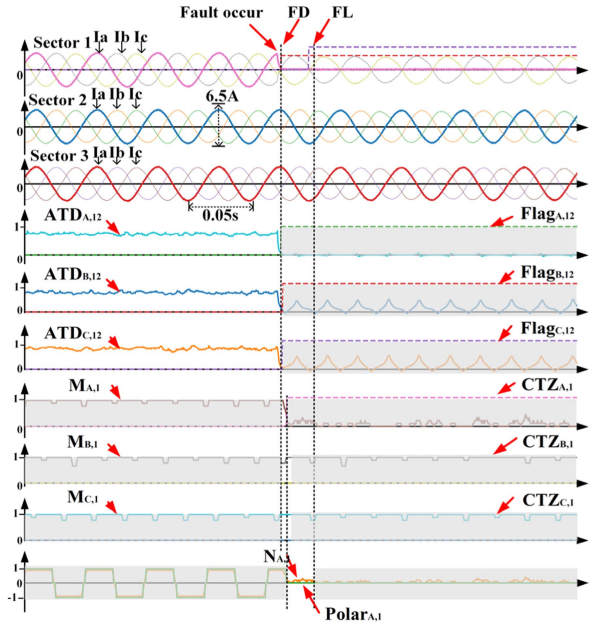

Fig. 10. Fault diagnosis process when T1T2 open circuit.

be distorted, which is significantly different from the current of other healthy sectors, while the phase current of healthy sectors remains highly similar. Therefore, after the fault occurs, $\text{ATD}_{\text{A},12}$, $\text{ATD}_{\text{B},12}$, and $\text{ATD}_{\text{C},12}$ decrease significantly and are below the threshold, as shown in subfigure 2. Because of the consistency between sectors, the $\text{ATD}_{\text{A},13}$, $\text{ATD}_{\text{B},13}$, $\text{ATD}_{\text{C},13}$ and $\text{ATD}_{\text{A},14}$, $\text{ATD}_{\text{B},14}$, $\text{ATD}_{\text{C},14}$ are also below the threshold after the fault. In this case, the fault can be detected and located in the first sector. The percentage of the three-phase current zero samples in the first sector is shown in subfigure 3. $M_{\text{A},1}$ is smaller than K_z, which means that phase A is faulty. If the two-phase switches are open at the same time, their CTZ signal changes are close to each other, with no more than ten sampling periods. Therefore, when $\text{CTZ}_{\text{A},1} = 1$, both $\text{CTZ}_{\text{B},1}$ and $\text{CTZ}_{\text{C},1}$ are 0 for ten sampling periods. Therefore, when $\text{CTZ}_{\text{A},1} = 1$, both $\text{CTZ}_{\text{B},1}$ and $\text{CTZ}_{\text{C},1}$ are 0 for ten sampling periods, which means that both phases B and C are healthy. Meanwhile, subfigure 4 shows that $\text{Polar}_{\text{A},1}$ becomes -1 after $\text{CTZ}_{\text{A},1}$, which means that the upper switch on sector 1 A phase is open and the fault classification is complete. The detection and fault sector location time are 0.08 fundamental waveform cycle. The exact location time is 0.41 fundamental waveform cycle, shown in subfigure 1.

B. Double OS Fault Diagnosis

Fig. 10 shows the diagnosis process of the first sector T1T2 switches open fault. After the fault occurs, the phase A current of the first sector is distorted. $\text{ATD}_{\text{A},12}$, $\text{ATD}_{\text{B},12}$, and $\text{ATD}_{\text{C},12}$ are quickly below the threshold. $\text{Flag}_{\text{A},12}$, $\text{Flag}_{\text{B},12}$, and $\text{Flag}_{\text{C},12}$ are set to 1, while the phase currents of other sectors remain unchanged, and the fault position is the first sector, as shown in subfigure 1, 2. In subfigure 3, $M_{\text{A},1}$ is rapidly lower than K_Z. After that, $M_{\text{B},1}$ and $M_{\text{C},1}$ maintain much higher than the threshold for ten sampling periods, which locates the fault at

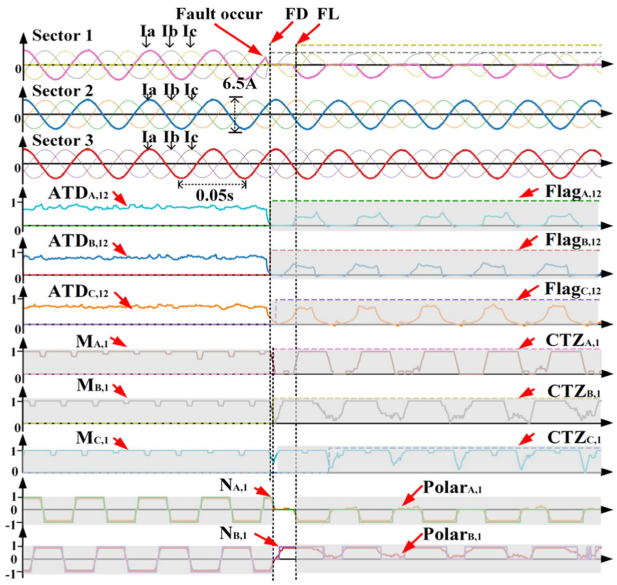

Fig. 11. Fault diagnosis process when T1T4 open circuit.

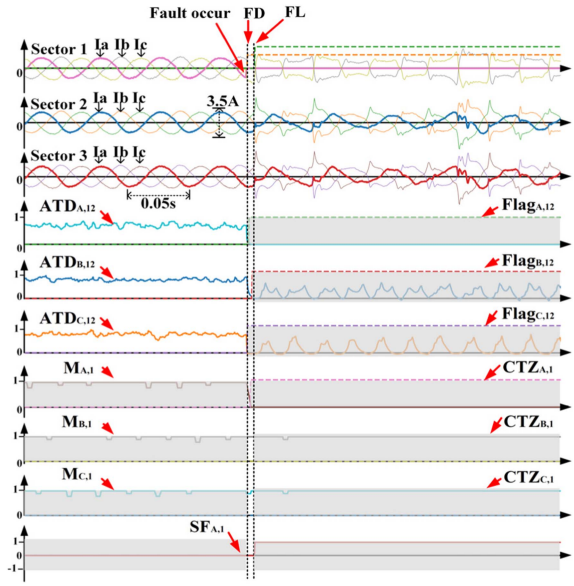

Fig. 12. Fault diagnosis process when the sector 1 A phase current sensor SL.

phase A of the first sector. In subfigure 4, $\mathrm{Polar}_{\mathrm{A},1}$ keeps 0 in the half current fundamental period after the $\mathrm{Flag}_{\mathrm{A},12} = 1$, which means that the upper and lower switches of phase A are at fault. The detection and fault sector location time of two switches on the same bridge is 0.07 fundamental wave cycle, and the accurate location time is 0.57 fundamental wave cycle.

Fig. 11 shows the diagnosis process of the first sector T1T4 switches open fault. The three-phase current in the first sector is distorted after the fault, $\mathrm{ATD}_{\mathrm{A},12}$, $\mathrm{ATD}_{\mathrm{B},12}$, and $\mathrm{ATD}_{\mathrm{C},12}$ are quickly below the threshold, and other sectors are almost not affected by the fault in the first sector, so the fault sector is the first, as shown in subfigure 1, 2. In subfigure 3, $M_{\mathrm{A},1}$, $M_{\mathrm{B},1}$ are rapidly lower than K_z, and $\mathrm{CTZ}_{\mathrm{A},1}$, $\mathrm{CTZ}_{\mathrm{B},1}$ become 1. When $\mathrm{CTZ}_{\mathrm{A},1} = 1$ and $\mathrm{CTZ}_{\mathrm{B},1} = 1$, $\mathrm{CTZ}_{\mathrm{C},1}$ is 0 for ten sampling periods, which means that A and B phase switch fails has occurred. Meanwhile, subfigure 4 shows that $\mathrm{Polar}_{\mathrm{B},1}$ becomes one after $\mathrm{CTZ}_{\mathrm{B},1} = 1$, which means that the lower switch on sector 1 B phase is open. Then, the $\mathrm{Polar}_{\mathrm{A},1}$ becomes -1 after $\mathrm{CTZ}_{\mathrm{A},1} = 1$, which means that the upper switch on the sector 1 A phase is open. Therefore, the fault switches are the upper switch of phase A and the lower switch of phase B. The detection and fault sector location time of two switches with different phases are 0.08 fundamental wave cycles, and the accurate positioning time is 0.53 fundamental wave cycles.

C. Current Sensor Fault Diagnosis

Fig. 12 shows the SL fault diagnosis of the A-phase current sensor in the first sector. Different from the OS fault, the feedback value of the faulty sensor is forced to be 0 after the sensor fault. The loss of the current sensor signal will produce large actual current distortion, which leads to large torque ripple as well as distortion of the normal sector phase current, but the phase current coincidence rate between the normal sectors is still high, as shown in Fig. 1. For the safety of the device, the

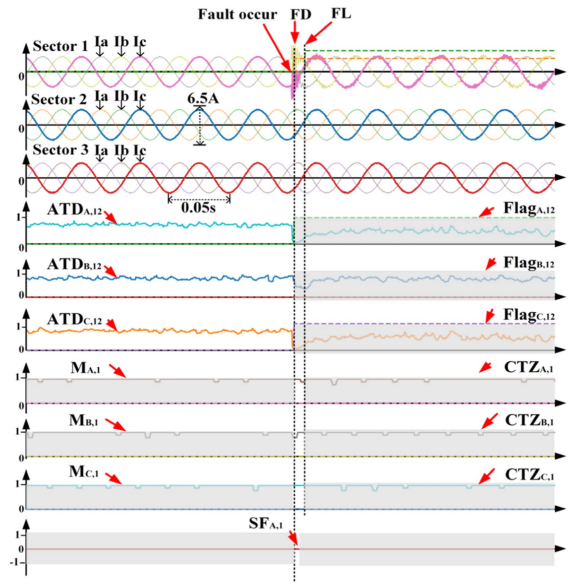

Fig. 13. Fault diagnosis process when the sector 1 A phase current sensor GV.

current sensor SL experiment is carried out at a lower current amplitude. In subfigures 2 and 3, $\mathrm{ATD}_{\mathrm{A},12}$, $\mathrm{ATD}_{\mathrm{B},12}$, $\mathrm{ATD}_{\mathrm{C},12}$ rapidly drop below the threshold after the fault occurs, while $\mathrm{Flag}_{\mathrm{A},12}$, $\mathrm{Flag}_{\mathrm{B},12}$, and $\mathrm{Flag}_{\mathrm{C},12}$ are set to 1. After the fault is detected, CTZ does not change for ten sampling periods. At the same time, $\mathrm{SF}_{\mathrm{A},1}$ becomes 1, which means that A phase current sensor SL. The detection and fault sector location time are 0.06 fundamental wave cycles, and the accurate fault location time is 0.16 fundamental wave cycles.

Fig. 13 shows the GV diagnosis of the A-phase current sensor in the first sector. After the fault, the feedback value of the fault sensor is 0.4 times the actual value. Since the feedback current of phase C is calculated by the feedback current of phase A and

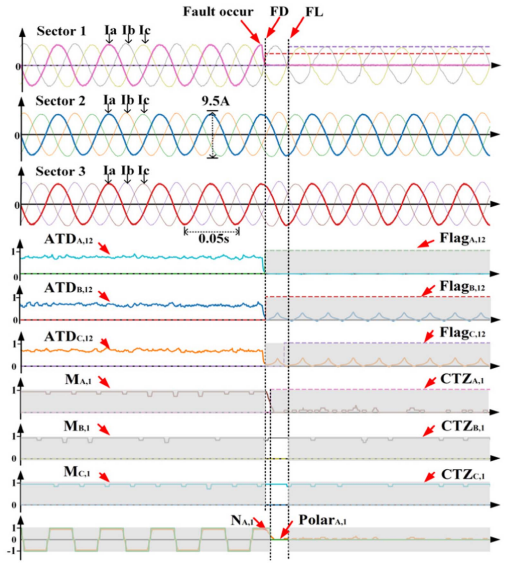

Fig. 14. Fault diagnosis process under different current amplitude.

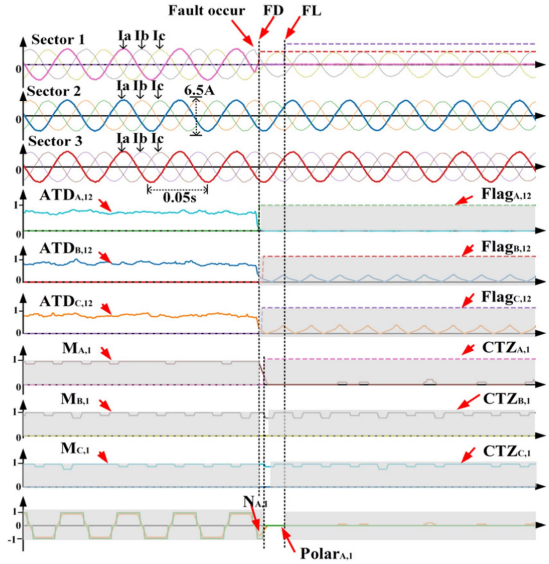

Fig. 15. Fault diagnosis process under different sampling frequency.

phase B, the feedback current of phase C is also 0.4 times the actual value. After the transient distortion, the phase current of the faulty sector and the health y sector still maintain a certain degree of coincidence, as shown in subfigure 1. In subfigures 2 and 3, $ATD_{A,12}$ and $ATD_{B,12}$ quickly fall below the threshold after the fault occurs, but $CTZ_{A,1}$, $CTZ_{B,1}$, and $CTZ_{C,1}$ are much higher than the threshold in the 20 sampling periods after the fault is detected, so the fault can be identified as a gain or zero drift fault in one of the sensors. The detection and fault sector location time are 0.06 fundamental wave cycles, and the accurate positioning time is 0.26 fundamental wave cycles. Further identification of the current sensor GV or ZO can be achieved by current loop output comparison.

D. Performance Evaluation Under Different Sample Frequency or Current Amplitude

Fig. 14 shows the diagnosis process of the first sector T1T2 switch open-circuit fault when the current amplitude is 9.5 A. A larger current amplitude means a larger difference between the faulty sector and the healthy sector. Compared with the small amplitude, the difference between the set threshold and one is larger, and the false alarm rate is lower on the basis of the unchanged diagnostic performance. $ATD_{A,12}$, $ATD_{B,12}$, $ATD_{C,12}$, $CTZ_{A,1}$, $CTZ_{B,1}$, $CTZ_{C,1}$ and $Polar_{A,1}$, $Polar_{B,1}$, $Polar_{C,1}$ have less fluctuation after failure. The detection and fault sector time are 0.07 fundamental wave cycles, and the accurate positioning time is 0.57 fundamental wave cycles.

Fig. 15 shows the diagnosis process of the first sector T1T2 switch open-circuit fault when the sampling frequency is 50 times the fundamental current frequency. The threshold is set to 0.13 after traversal based on different sampling frequencies. The fault detection and fault sector location time are 0.08 fundamental cycles, and the accurate positioning time is 0.58 fundamental cycles. It is worth that due to the large gap between post-fault and normal $ATD_{A,12}$, $ATD_{B,12}$, $ATD_{C,12}$, well-fault diagnosis

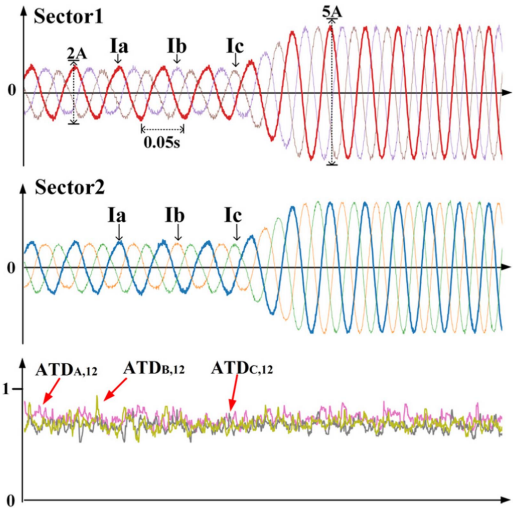

Fig. 16. Fault diagnosis process under phase current mutation.

performance can still be achieved through the corresponding design of the threshold.

E. Performance Evaluation Under Transient Working Conditions

The current and reference speed mutation are tested to prove the robustness of the proposed diagnostic method. In Fig. 16, the phase currents of each sector change from 2 to 5 A at 300 r/min. In Fig. 17, the reference speed changes from 300 to 500 r/min under 5 A current amplitude. The transient current fluctuation and mutation of system frequency almost have no effect on $ATD_{A,12}$, $ATD_{B,12}$, $ATD_{C,12}$.

F. Comparison of Previous Methods

For a multisector PMSM system, each sector is regarded as an independent three-phase PMSM, and the traditional method

TABLE IV
COMPARISON WITH PREVIOUS METHODS

Diagnostic Method	Detection and Fault sector Location Time	Robustness	Tuning Efforts	Cost	Sensitive to System Parameters	Fault Category
Current signal-based method [34]	>1 cycle	Low	Medium	Low	Low	Only Switch
Model-based method [35]	1/4 cycle	High	Medium	Low	High	Only Switch
Machine learning method [25]	>1 cycle	High	High	High	Low	Switch and Sensor
Proposed method	<1/10cycle	High	Medium	Low	Low	Switch and Sensor

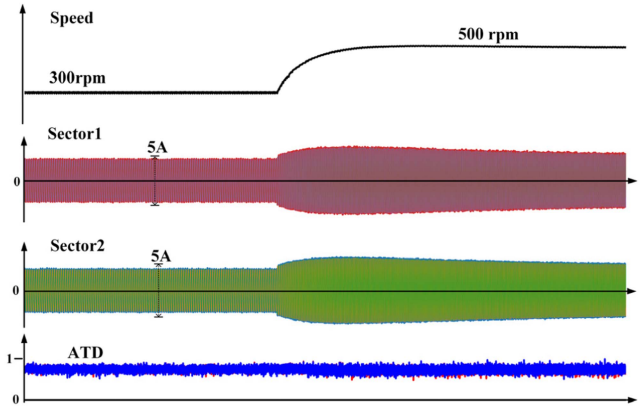

Fig. 17. Fault diagnosis process under speed mutation.

is useful for fault diagnosis. In this section, the performance of the proposed diagnostic method is compared with the previous methods, such as detection and fault sector location time, robustness, cost, sensitivity to system parameters, tuning efforts, and fault category. The results are shown in Table IV. Although the threshold and feature parameters design has been fairly conservative, the proposed method can detect and locate the switch and sensor fault to fault sector within 0.1 current fundamental period, which is unavailable before. It is worth noting that for the multisector PMSM drive, fault-tolerant control is mostly carried out by removing the fault sector in the case of high security and control performance. Therefore, as fast as possible detection and fault sector positioning for multisector PMSM drive is significant. In addition, the proposed method can identify $21*N$ kinds of switch faults and $7*N$ kinds of current sensor faults without additional sensors and circuits. At the same time, the proposed method does not depend on system parameters and is robust to speed and current changes. It can be seen from Table IV, in addition to the superior performance of fault identification and fault sector location, the proposed method can achieve a better performance for the abovementioned indexes, while the previous methods have one to multiple shortcomings.

V. CONCLUSION

This article proposes an ML-based fault diagnosis method for OS and current sensor faults, which improves the speed of fault detection and fault sector location in the MPMSM system. First, compared with the traditional Euclidean and cosine distance, an ATD is designed to more obviously reflect the dissimilarity of the same phase current between the healthy and faulty sectors. Second, its value under different fault conditions is theoretically analyzed, which provides a reference for threshold setting and reduces the tuning effort. The ATD and reasonable threshold reference ensure high immunity to the false alarm rate. The detection time of the faults is within 0.1 current fundamental cycles by using the proposed method, which is far less than the previous method. Finally, the set of the sector ensures simultaneous fault sector location and fault detection. The set of CTZ, SF, and polar can accurately distinguish 28 kinds of OS and current sensor faults in the fault sector. The proposed method is easy to implement online without extra sensors and has a low computational cost. In addition, it does not require the mathematical model of the motor. The Fault diagnosis is carried out through structural characteristics, which means that the method is naturally robust to the speed and current variation.

REFERENCES

[1] D. Jiang, K. Liu, Z. Liu, Q. Wang, Z. He, and R. Qu, "Four-module three-phase PMSM drive for suppressing vibration and common-mode current," *IEEE Trans. Ind. Appl.*, vol. 57, no. 5, pp. 4874–4883, Sep./Oct. 2021.

[2] Y. Xu, W. Zhang, Y. Huang, and J. Zou, "Multisector three-phase PMSM drive system with low-frequency and high-frequency PWM noise," *IEEE J. Emerg. Sel. Topics Power Electron.*, vol. 10, no. 2, pp. 1639–1648, Apr. 2022.

[3] G. Wu, S. Huang, Q. Wu, F. Rong, C. Zhang, and W. Liao, "Robust predictive torque control of N∗3-phase PMSM for high-power traction application," *IEEE Trans. Power Electron.*, vol. 35, no. 10, pp. 10799–10809, Oct. 2020.

[4] S. Yang, D. Xiang, A. Bryant, P. Mawby, L. Ran, and P. Tavner, "Condition monitoring for device reliability in power electronic converters: A review," *IEEE Trans. Power Electron.*, vol. 25, no. 11, pp. 2734–2752, Nov. 2010.

[5] S. Khojet El Khil, I. Jlassi, A. J. Marques Cardoso, J. O. Estima, and N. Mrabet-Bellaaj, "Diagnosis of open-switch and current sensor faults in PMSM drives through stator current analysis," *IEEE Trans. Ind. Appl.*, vol. 55, no. 6, pp. 5925–5937, Nov./Dec. 2019.

[6] G. Zhang, G. Wang, G. Wang, J. Huo, L. Zhu, and D. Xu, "Fault diagnosis method of current sensor for permanent magnet synchronous motor drives," *Int. Power Electron. Conf., IPEC-Niigata—ECCE Asia*, 2018, pp. 1206–1211.

[7] Z. Gao, C. Cecati, and S. X. Ding, "A survey of fault diagnosis and fault-tolerant techniques—Part I: Fault diagnosis with model-based and signal-based approaches," *IEEE Trans. Ind. Electron.*, vol. 62, no. 6, pp. 3757–3767, Jun. 2015.

[8] Z. Gao, C. Cecati, and S. X. Ding, "A survey of fault diagnosis and fault-tolerant techniques—Part II: Fault diagnosis with knowledge-based and hybrid/active approaches," *IEEE Trans. Ind. Electron.*, vol. 62, no. 6, pp. 3768–3774, Jun. 2015.

[9] Q.-T. An, L. Sun, and L.-Z. Sun, "Current residual vector-based open-switch fault diagnosis of inverters in PMSM drive systems," *IEEE Trans. Power Electron.*, vol. 30, no. 5, pp. 2814–2827, May 2015.

[10] B. Gou, X. Ge, S. Wang, X. Feng, J. B. Kuo, and T. G. Habetler, "An open-switch fault diagnosis method for single-phase PWM rectifier using a model-based approach in high-speed railway electrical traction drive system," *IEEE Trans. Power Electron.*, vol. 31, no. 5, pp. 3816–3826, May 2016.

[11] W. Huang, J. Du, W. Hua, K. Bi, and Q. Fan, "A hybrid model-based diagnosis approach for open-switch faults in PMSM drives," *IEEE Trans. Power Electron.*, vol. 37, no. 4, pp. 3728–3732, Apr. 2022.

[12] M. Manohar and S. Das, "Current sensor fault-tolerant control for direct torque control of induction motor drive using flux-linkage observer," *IEEE Trans. Ind. Informat.*, vol. 13, no. 6, pp. 2824–2833, Dec. 2017.
[13] D. Zhou, S. Yang, and Y. Tang, "A voltage-based open-circuit fault detection and isolation approach for modular multilevel converters with model-predictive control," *IEEE Trans. Power Electron.*, vol. 33, no. 11, pp. 9866–9874, Nov. 2018.
[14] J. Hang, J. Zhang, M. Cheng, and S. Ding, "Detection and discrimination of open-phase fault in permanent magnet synchronous motor drive system," *IEEE Trans. Power Electron.*, vol. 31, no. 7, pp. 4697–4709, Jul. 2016.
[15] C. Cecati, A. O. Di Tommaso, F. Genduso, R. Miceli, and G. Ricco Galluzzo, "Comprehensive modeling and experimental testing of fault detection and management of a nonredundant fault-tolerant VSI," *IEEE Trans. Ind. Electron.*, vol. 62, no. 6, pp. 3945–3954, Jun. 2015.
[16] F. R. Salmasi, "A self-healing induction motor drive with model free sensor tampering and sensor fault detection, isolation, and compensation," *IEEE Trans. Ind. Electron.*, vol. 64, no. 8, pp. 6105–6115, Aug. 2017.
[17] C. Cecati, A. O. Di Tommaso, F. Genduso, R. Miceli, and G. Ricco Galluzzo, "Comprehensive modeling and experimental testing of fault detection and management of a nonredundant fault-tolerant VSI," *IEEE Trans. Ind. Electron.*, vol. 62, no. 6, pp. 3945–3954, Jun. 2015.
[18] J. O. Estima, N. M. A. Freire, and A. J. M. Cardoso, "Recent advances in fault diagnosis by Park's vector approach," in *Proc. IEEE Workshop Elect. Mach. Des. Control Diagnosis*, Mar. 2013, pp. 279–288.
[19] Z. Li, Y. Gao, X. Zhang, B. Wang, and H. Ma, "A model-data-hybrid-driven diagnosis method for open-switch faults in power converters," *IEEE Trans. Power Electron.*, vol. 36, no. 5, pp. 4965–4970, May 2021.
[20] Y. Xia, Y. Xu, and B. Gou, "A data-driven method for IGBT open-circuit fault diagnosis based on hybrid ensemble learning and sliding-window classification," *IEEE Trans. Ind. Informat.*, vol. 16, no. 8, pp. 5223–5233, Aug. 2020.
[21] Z. Huang, Z. Wang, X. Yao, and H. Zhang, "Multi-switches fault diagnosis based on small low-frequency data for voltage-source inverters of PMSM drives," *IEEE Trans. Power Electron.*, vol. 34, no. 7, pp. 6845–6857, Jul. 2019.
[22] S. Ye, J. Jiang, J. Li, Y. Liu, Z. Zhou, and C. Liu, "Fault diagnosis and tolerance control of five-level nested NPP converter using wavelet packet and LSTM," *IEEE Trans. Power Electron.*, vol. 35, no. 2, pp. 1907–1921, Feb. 2020.
[23] Y. Xia and Y. Xu, "A transferrable data-driven method for IGBT open-circuit fault diagnosis in three-phase inverters," *IEEE Trans. Power Electron.*, vol. 36, no. 12, pp. 13478–13488, Dec. 2021.
[24] S. Khojet El Khil, I. Jlassi, A. J. Marques Cardoso, J. O. Estima, and N. Mrabet-Bellaaj, "Diagnosis of open-switch and current sensor faults in PMSM drives through stator current analysis," *IEEE Trans. Ind. Appl.*, vol. 55, no. 6, pp. 5925–5937, Nov./Dec. 2019.
[25] B. Gou, Y. Xu, Y. Xia, Q. Deng, and X. Ge, "An online data-driven method for simultaneous diagnosis of IGBT and current sensor fault of three-phase PWM inverter in induction motor drives," *IEEE Trans. Power Electron.*, vol. 35, no. 12, pp. 13281–13294, Dec. 2020.
[26] F. Xiong, Y. Xiao, Z. Cao, Y. Wang, J. T. Zhou, and J. Wu, "ECML: An ensemble cascade metric-learning mechanism toward face verification," *IEEE Trans. Cybern.*, vol. 52, no. 3, pp. 1736–1749, Mar. 2022.
[27] Y. Feng, Y. Yuan, and X. Lu, "Person reidentification via unsupervised cross-view metric learning," *IEEE Trans. Cybern.*, vol. 51, no. 4, pp. 1849–1859, Apr. 2021.
[28] G. Cheng, C. Yang, X. Yao, L. Guo, and J. Han, "When deep learning meets metric learning: Remote sensing image scene classification via learning discriminative CNNs," *IEEE Trans. Geosci. Remote Sens.*, vol. 56, no. 5, pp. 2811–2821, May 2018.
[29] W. Zuo et al., "Distance metric learning via iterated support vector machines," *IEEE Trans. Image Process.*, vol. 26, no. 10, pp. 4937–4950, Oct. 2017.
[30] X. Yang, P. Zhou, and M. Wang, "Person reidentification via structural deep metric learning," *IEEE Trans. Neural Netw. Learn. Syst.*, vol. 30, no. 10, pp. 2987–2998, Oct. 2019.
[31] F. Wu and J. Zhao, "Current similarity analysis-based open-circuit fault diagnosis for two-level three-phase PWM rectifier," *IEEE Trans. Power Electron.*, vol. 32, no. 5, pp. 3935–3945, May 2017.
[32] D. Zhou, H. Qiu, S. Yang, and Y. Tang, "Submodule voltage similarity-based open-circuit fault diagnosis for modular multilevel converters," *IEEE Trans. Power Electron.*, vol. 34, no. 8, pp. 8008–8016, Aug. 2019.
[33] Y. Demir and M. Aydin, "A novel asymmetric and unconventional stator winding configuration and placement for a dual three-phase surface PM motor," *IEEE Trans. Magn.*, vol. 53, no. 11, Nov. 2017, Art. no. 8111805.
[34] C. Cecati, A. O. Di Tommaso, F. Genduso, R. Miceli, and G. Ricco Galluzzo, "Comprehensive modeling and experimental testing of fault detection and management of a nonredundant fault-tolerant VSI," *IEEE Trans. Ind. Electron.*, vol. 62, no. 6, pp. 3945–3954, Jun. 2015.
[35] I. Jlassi, J. O. Estima, S. Khojet El Khil, N. Mrabet Bellaaj, and A. J. Marques Cardoso, "Multiple open-circuit faults diagnosis in back-to-back converters of PMSG drives for wind turbine systems," *IEEE Trans. Power Electron.*, vol. 30, no. 5, pp. 2689–2702, May 2015.

Yutao Du (Student Member, IEEE) received the B.S. degree from the China University of Petroleum, Tsingtao, China, in 2017 and the M.S. degree from Beihang University, Beijing, China, in 2020, both in electrical engineering. He is currently working toward the Ph.D. degree in power electronics and electrical drives with the State Key Laboratory of Power System, Department of Electrical Engineering, Tsinghua University, Beijing, China.

His current research interests include fault diagnosis and high-performance control of motor system.

Chi Li (Member IEEE) received the B.S. degree in electrical engineering from Tsinghua University, Beijing, China, in 2012 and the M.S. and Ph.D. degrees in electrical engineering from Virginia Tech, Blacksburg, VA, USA, in 2015 and 2018, respectively.

From 2012 to 2018, he was a Research Assistant with the Center for Power Electronics Systems (CPES), Virginia Tech. In 2018, he returned to Tsinghua University and he is currently an Assistant Researcher with the Department of Electrical Engineering, Tsinghua University. His research interests include control and stability of grid-tied power electronics converters and systems, and solid-state transformers.

Zedong Zheng (Senior Member IEEE) was born in Shandong, China, in 1980. He received the B.S. and Ph.D. degrees in electrical engineering from the Department of Electrical Engineering, Tsinghua University, Beijing, China, in 2003 and 2008, respectively.

He is currently an Associate Professor with the Department of Electrical Engineering, Tsinghua University. His current research interests include power electronics converters and high-performance motor control systems.